ADVANCED MATERIALS INTERFACES

www.advmatinterfaces.de

The Exploration of Carrier Behavior in the Inverted Mixed Perovskite Single-Crystal Solar Cells

Yuan Huang, Yu Zhang, Junlu Sun, Xiaoge Wang, Junliang Sun, Qi Chen, Caofeng Pan, and Huanping Zhou**

Perovskite single crystal (PSC) possesses fewer bulk defects than the polycrystalline film counterpart, which has received extensive attention in a number of optoelectronic device applications. But the management of carrier behavior in an efficient solar cell based on PSC is not reported yet. Here, the carrier behavior within the device based on the ITO/NiO_x/$(FAPbI_3)_{0.85}(MAPbBr_3)_{0.15}$/$TiO_2$/Ag structure (FA = $CH(NH_2)_2^+$, MA = $CH_3NH_3^+$), in which the mixed PSC is successfully implemented into solar cells for the first time, is investigated. The PSC films with lateral dimension from 500 µm to 2 mm and thickness over tens of micrometers, are obtained through the polydimethylsiloxane-assisted solvent evaporation method. The highest power conversion efficiency derived from the present device approaches 12.18%. It is revealed that the surface roughness and thickness of PSC, the operation temperature and thickness of transport layers, and the interfaces of transport layers/PSC largely impact the carrier extraction and device performance of the perovskite single-crystal solar cell (PSCSC). This work indicates that the carrier behavior in the absorber layer and transport layer has large impact on the performance of PSCSCs, while the underlying design rule represents an important step to advance the PSCSCs and other optoelectronic devices.

1. Introduction

Owing to the superior optoelectronic properties, for example, long carrier lifetime,[1] high absorption coefficient,[2] and exceptional defect tolerance,[3] organic/inorganic hybrid perovskites have been emerged as the most fascinating semiconductor for the application in various fields,[4–7] particularly in solar cells.[8] In contrast to the polycrystalline films, perovskite single crystals (PSC) possess the advantages of smaller trap densities (≈10^{10} cm^{-3}) and better transport properties (≈60 cm^2 V^{-1} s^{-1}).[9,10] These characteristics will potentially enable the corresponding optoelectronic devices with improved performance, and it has been predicted that the perovskite single-crystal solar cells (PSCSCs) could achieve 25% power conversion efficiency (PCE).[11,12] Different from the inorganic single crystals (e.g., Si, GaAs), an additional attribute of organic–inorganic perovskite single crystals is the ease of their synthetic method that varied from the antisolvent vapor-assisted crystallization,[10,13] the inverse temperature crystallization,[14,15] the temperature-lowering method[9,16,17] based on solution, etc. Therefore, it is of extreme interest to investigate PSCSC, which may facilitate fundamental understanding regarding intrinsic materials property and device physics to develop most promising perovskite solar cells.

To enable an efficient PSCSC, research efforts are focused on realizing high-quality perovskite single crystals with desired dimension, as well as the optimum device structure through exquisite control on the interfaces. Initially, an inverted PSCSC (ITO/PEDOT:PSS/$CH_3NH_3PbI_3$/PCBM/ZnO/Al) has been demonstrated with a 1.73% PCE, while the droplet-pinned crystallization method induced an incomplete coverage of $MAPbI_3$ (MA = $CH_3NH_3^+$) single-crystal arrays with width of tens of micrometers and the thickness over the range from about 300 nm to about 3 µm.[18] A lateral PSCSC based on the

Y. Huang, Y. Zhang, Prof. H. P. Zhou
Department of Materials Science and Engineering
Department of Energy and Resources Engineering
College of Engineering
Peking University
Beijing 100871, P. R. China
E-mail: happy_zhou@pku.edu.cn

J. L. Sun, Prof. C. F. Pan
Beijing Institute of Nanoenergy and Nanosystems
Chinese Academy of Sciences
Beijing 100083, P. R. China
E-mail: cfpan@binn.cas.cn

X. G. Wang, Prof. J. L. Sun
College of Chemistry and Molecular Engineering
Peking University
Beijing 100871, P. R. China

Prof. Q. Chen
School of Materials Science and Engineering
Beijing Institute of Technology
Beijing 100081, P. R. China

The ORCID identification number(s) for the author(s) of this article can be found under https://doi.org/10.1002/admi.201800224.

DOI: 10.1002/admi.201800224

Au/bulk $MAPbI_3$ single crystal (≈50 µm channel length)/Au structure delivered 1.88% PCE at room temperature without employing carrier transport layers.[19] Subsequently, a single-crystal film with thicknesses of tens of micrometers, and lateral dimensions ranging from hundreds of micrometers to 3 mm were obtained via the cavitation-triggered asymmetrical crystallization strategy. By employing the structure of FTO/TiO_2/$MAPbBr_3$/Au, the PSCSC with the thinnest film (1 µm in thickness) produced the highest efficiency (6.53%).[20] Thin single crystals with substantially larger lateral size (6 mm × 8 mm) and the controllable thickness of micrometers (16 µm) were obtained by the space-limited inverse temperature crystallization, and achieved 7.11% PCE when implemented in the FTO/TiO_2/$MAPbBr_3$/Spiro/Au structure.[21] A PCE of 8.78% was demonstrated for the FTO/TiO_2/$MAPbI_3$/Spiro/Ag PSCSC,[22] in which the $MAPbI_3$ film with the thickness varying from few micrometers to 200 µm was obtained by the space confined growth (SCG). The published highest efficiency of PSCSC (ITO/PTAA/$MAPbI_3$/PCBM/C_{60}/BCP/Cu) was 17.8%,[23] where hydrophobic interface confined lateral growth method was used to synthesize the millimeter-size single crystal with thickness of 10–20 µm. It points out that the perovskite single-crystal film with desired lateral size and thickness is the prerequisite to an efficient PSCSC, while good carrier extraction between perovskite/transport materials would further improve the photovoltaic efficiency. Despite the progress on the intriguing strategies to boost the device performance, a profound understanding of PSCSC in the perspective of the entire carrier dynamics pathway is necessary.

Herein, we developed a polydimethylsiloxane (PDMS)-assisted solvent evaporation crystallization method to grow mixed halide perovskite single-crystal films, namely, $(FAPbI_3)_{0.85}(MAPbBr_3)_{0.15}$ (FA = $CH(NH_2)_2^+$) for the first time.[24] The carrier behavior in the single-crystal solar cells (ITO/NiO_x/$(FAPbI_3)_{0.85}(MAPbBr_3)_{0.15}$/$TiO_2$/Ag) was thoroughly studied through controlling the thickness and roughness of single-crystal films, the operation temperature and thickness of transport layers, the interface of perovskite and electron transport layer (ETL)/ hole transport layer (HTL). The thinner and smoother surface of single crystal, accompanying with the implementation of TiO_2 transport materials improved the carrier extraction and the resulting PCE of the devices. The hole extraction at the NiO_x/single-crystal interface was also enhanced by controlling the evaporation rate of perovskite solution to avoid the formation of insulating blocks. This leads to a 12.18% PCE in an inverted device architecture, which was also among the high-efficiency PSCSCs up till now. The detailed discussion about the device structure lays the foundation for the further improvement of PSCSCs and the performance of other optoelectronic devices, such as light-emitting diodes, field-effect transistors, and photoconductive devices.

2. Results and Discussion

2.1. PDMS-Assisted Solvent Evaporation Crystallization

We grew $(FAPbI_3)_{0.85}(MAPbBr_3)_{0.15}$ single crystals with the PDMS-assisted solvent evaporation crystallization method, as described in **Figure 1**a. One piece of PDMS with the thickness of 2 mm and an area of 3 cm × 3 cm was placed on the NiO_x/ITO substrate, followed by a quick injection of perovskite solution between PDMS/substrate. After heating the substrate at 80 °C for 2 h, certain amount of regular hexagonal $(FAPbI_3)_{0.85}(MAPbBr_3)_{0.15}$ single crystals were crystallized on the substrates. The growth details can be found in the Experimental Section.

The quality of $(FAPbI_3)_{0.85}(MAPbBr_3)_{0.15}$ perovskite single crystals can be improved during the crystal growth by carefully controlling the solvent evaporation rate and thus the

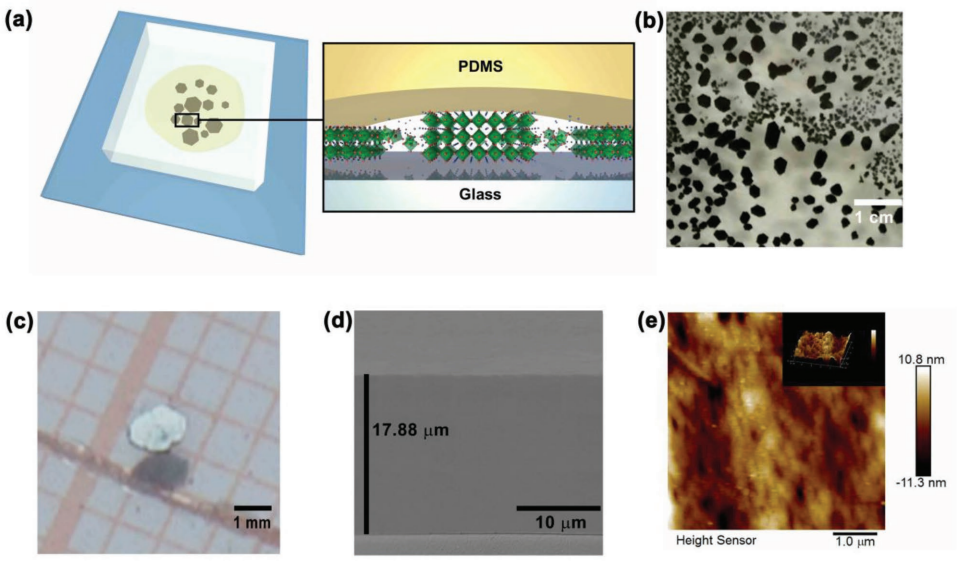

Figure 1. a) The growth mechanism of $(FAPbI_3)_{0.85}(MAPbBr_3)_{0.15}$ single crystals by the PDMS-assisted solvent evaporation crystallization method; photographs of b) single crystals under one piece of PDMS and c) one magnified crystal; the microscopy image of one regular single crystal: d) the cross-sectional scanning electron microscope (SEM) image and e) the atomic force microscope (AFM) image by scanning an area of 5 × 5 µm^2.

supersaturation degree. It has been a big challenge to grow single-crystal film with broad absorption such as $MAPbI_3$, which may result from the different solubility of MAI and PbI_2, and probably the intrinsic anisotropic growth of tetragonal phase.[20] The $MAPbX_3$ (X = I, Br, Cl) single-crystal film with adjustable thickness from nanometers to micrometers can be readily obtained by SCG strategy. However, tetragonal $MAPbI_3$ single crystal with oblique angles at the edges exhibits substantially smaller lateral size than $MAPbX_3$ (X = Br, Cl) single crystal under the same growth condition.[25] The characteristic of PDMS allows the growth of iodide-based perovskite single crystal with relatively desired dimension and quality. PDMS is inherently high porosity that facilitates a gradual evaporation of solvent during crystallization, which may be particularly suitable for the growth of iodide-based perovskite single crystal. And the dimension of the single crystals could be controlled by the solvent evaporation rate. The obtained $(FAPbI_3)_{0.85}(MAPbBr_3)_{0.15}$ perovskite single crystal with thickness of micrometers (≈10–50 μm) ranged from 500 μm to 2 mm in lateral size, as shown in Figure 1b. Figure 1c presents a typical single crystal with a lateral size of ≈1 mm, while the surface of single crystal captured by the camera showed nearly mirror-like reflection, indicative of the relative smooth surface based on this growth method. The improved single-crystal surface quality, when compared with the thickness-controllable method,[22] was likely attributed to the dewetting interface of PDMS/perovskite, whereas the surface of single crystal was protected from mechanical damage when PDMS was teared from the perovskite single crystal. A typical single-crystal film with thickness of 17.88 μm is shown in Figure 1d. The atomic force microscope (AFM) images of perovskite single-crystal surface showed a small root-mean-square roughness (0.74 nm) with a scanning area of 5 × 5 μm^2 (Figure 1e). Therefore, we considered that the mixed iodide perovskite single-crystal film derived from the PDMS-assisted solvent evaporation crystallization method had well-defined shape and respectable dimension. The combination of the suitable dimension and the broad absorption of mixed iodide perovskite ($(FAPbI_3)_{0.85}(MAPbBr_3)_{0.15}$) could be beneficial to the fabrication of efficient single-crystal solar cells.

The crystal quality and optoelectronic properties of $(FAPbI_3)_{0.85}(MAPbBr_3)_{0.15}$ were characterized. We grounded the $(FAPbI_3)_{0.85}(MAPbBr_3)_{0.15}$ crystals bladed from the slides, and carried out the powder XRD measurement. The diffraction peak at 14°, 28°, and 32° (**Figure 2**a) corresponds to the (001), (002), and (012) diffraction peak of cubic $(FAPbI_3)_{0.85}(MAPbBr_3)_{0.15}$.[26] Meanwhile, the clear (hk0) diffraction pattern from single-crystal XRD measurement indicated the high quality of single crystal (Figure 2b). According to Figure 2c, the cutoff absorption wavelength of single crystal was 825 nm, and the PL emission peak was located at 775 nm. The bandgap of the single crystal was near 1.50 eV, which was similar to the published value.[26] The confocal laser scanning fluorescence picture of a $(FAPbI_3)_{0.85}(MAPbBr_3)_{0.15}$ single crystal is shown in Figure 2d, and the uniformly distributed signal indicated its relatively pure phase. To detect the transport properties of single crystal, we conducted time-resolved photoluminescence (TRPL) measurement of a representative single crystal. Accordingly, the fitted bulk carrier lifetime (τ) was 1.96 μs (Figure 2e). The hole mobility (μ_h) of a typical single crystal, estimated from space-charge-limited current (SCLC) measurement, was 21.69 $cm^2\ V^{-1}\ s^{-1}$ according to the Mott–Gurney law $J_D = 9\varepsilon\varepsilon_0\mu V^2/8L^3$,[27] as shown in Figure 2f. Therefore, a diffusion length (L_D) of 10.50 μm was derived from the equation $L_D = (k_B T\mu\tau/e)^{1/2}$.[10] Meanwhile, we obtained the trap density of 2.16 × 10^{13} cm^{-3} based on the formula $V_{TFL} = en_t L^2/2\varepsilon\varepsilon_0$, indicating the high quality of single-crystal film, in contrast to the polycrystalline counterpart with the trap density around 4 × 10^{15} cm^{-3}.[28] All the characterizations demonstrated the high quality and good transport property of the single crystal synthesized by PDMS-assisted solvent evaporation method.

We grew single-crystal films on the NiO_x/ITO substrate and fabricated TiO_2 layer through the atomic layer deposition (ALD) on the upper surface of single crystal followed by thermal evaporation of Ag to employ an inverted configuration. The cross-sectional scanning electron microscope (SEM) images of the NiO_x/$(FAPbI_3)_{0.85}(MAPbBr_3)_{0.15}$ and $(FAPbI_3)_{0.85}(MAPbBr_3)_{0.15}$ /TiO_2 interfaces are listed in **Figure 3**a,b, respectively, which indicated the uniform thickness of NiO_x (≈95 nm) and TiO_2 (≈66 nm) layer. Figure 3c showed the energy diagram of the single-crystal solar cells, and the resulting *J*–*V* curve with the highest efficiency is listed in Figure 3d, whereas the thickness of single crystal was about 24.50 μm (Figure S1, Supporting Information). The corresponding photovoltaic parameters, including short current density (J_{SC}), open voltage (V_{OC}), fill factor (FF), shunt resistance (R_{Sh}), series resistance (R_S), and PCE were 23.14 mA cm^{-2}, 1.03 V, 0.51, 0.53 kΩ cm^2, 19.31 Ω cm^2, and 12.18%, respectively. We took the *J*–*V* curve from the device with the best performance to study the power as a function of resistance. As described elsewhere,[29] for a solar cell with moderate values of series resistance (R_S) and large shunt resistance (R_{Sh}), the maximum output power (P_{max}) may be approximated as the power in the absence of series resistance minus the power lost in the series resistance, presented as Equation (1), where *P* is the product of V_{OC} and J_{SC}.

$$P_{max} \cong J_{SC}V_{OC} - J_{SC}^2 R_S = P\left(1 - J_{SC}R_S/V_{OC}\right) \quad (1)$$

Accordingly, the calculated P_{max} was 13.49 mW, corresponding to the PCE of 13.49%, which was close to the values (12.18%) obtained in *J*–*V* measurement. On the other hand, the loading external resistance is pertinent to the power output. The maximum power output is achieved by adjusting the external resistance equal to the characteristic resistance (R_{CH}) of the solar cell, which is the output resistance of a solar cell at its maximum power point, namely, $R_{CH} = V_{mp}/I_{mp}$ (wherein V_{mp} is the voltage at maximum power point; I_{mp} is the current at maximum power point). When the solar cell operates at its maximum power point, it delivers the maximum power (12.18 mW) to the load.

Compared to that of the bromide perovskite single-crystal-based devices, these values manifested as substantially improved short current density, as a result from the broad absorption from iodide perovskites.[20,21] We further found that in contrast to other iodide perovskite single-crystal solar cells,[22] the V_{OC} in the present cell was improved significantly. Generally, the n-i-p structure (e.g., TiO_2/perovskite/Spiro-OMeTAD) based perovskite solar cell delivers a comparably higher V_{OC} than that based on the p-i-n structure (e.g., NiO_x/perovskite/TiO_2).[30] We

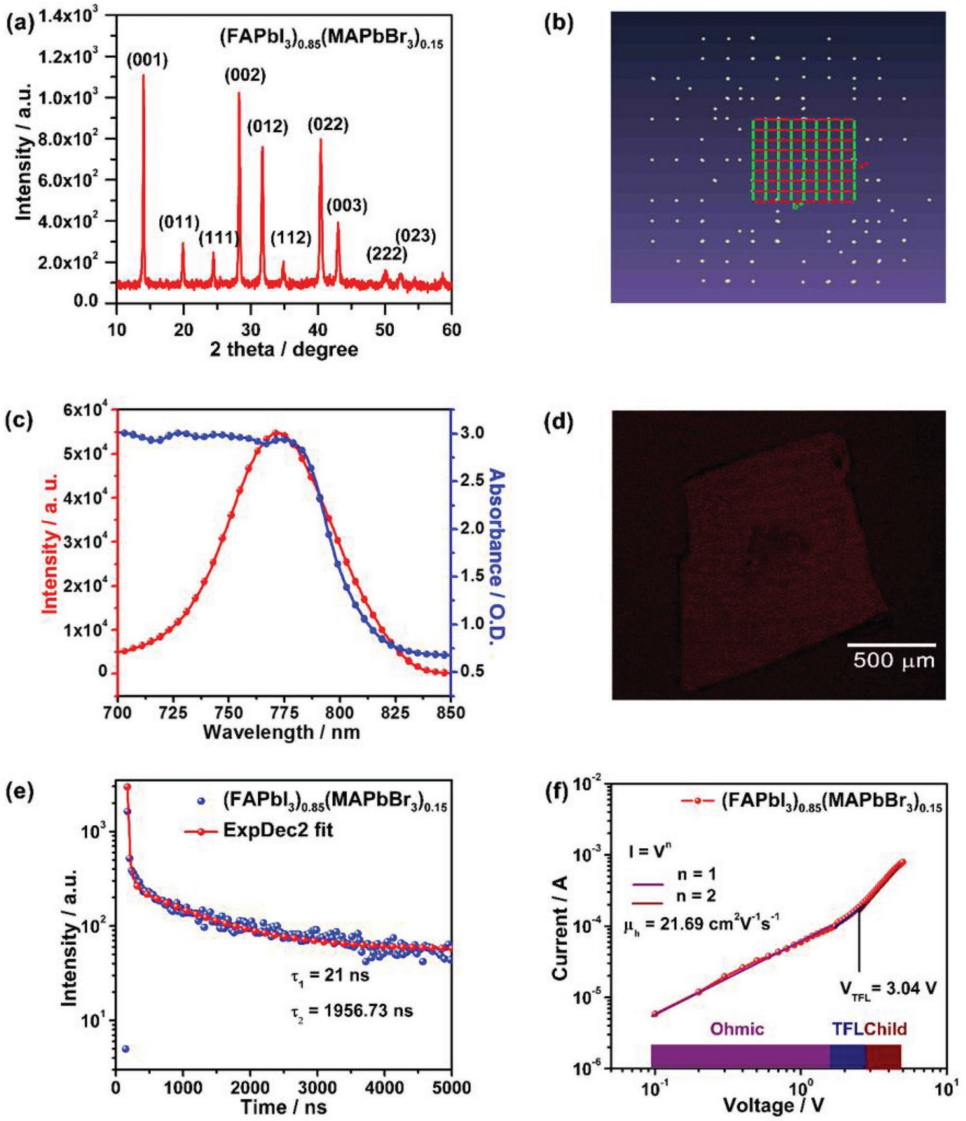

Figure 2. The characterization of $(FAPbI_3)_{0.85}(MAPbBr_3)_{0.15}$ single crystal. a) The powder X-ray diffraction (XRD) patterns; b) the (hk0) diffraction pattern; c) the absorption and photoluminescence (PL) emission spectra; d) the confocal laser scanning fluorescence picture; e) the time-resolved photoluminescence (TRPL) spectrum; and f) the *J–V* curve of ITO/NiO_x/$(FAPbI_3)_{0.85}$ $(MAPbBr_3)_{0.15}$ single crystal/Au device.

consider both NiO_x substrate for single-crystal direct growth and the compact TiO_2 layer on the surface of single crystal which leads to the good interface contact for extraction and suppressed recombination. Compared to the PSCSC based on the ITO/PTAA/$MAPbI_3$/PCBM/C_{60}/BCP/Cu device,[23] the main efficiency loss came from relatively smaller fill factor, which may be improved by reducing the thickness and surface defect of single crystal. Therefore, the $(FAPbI_3)_{0.85}(MAPbBr_3)_{0.15}$ single-crystal film with desired quality as well as good carrier extraction allows the high-efficiency single-crystal solar cells. To our understanding, it is the first time to report mixed perovskite based PSCSCs, in which the particular composition, namely, $(FAPbI_3)_{0.85}(MAPbBr_3)_{0.15}$ has the greatest potential to realize the highest performance perovskite solar cells.

The proposed schematic diagram of the working mechanism for ITO/NiO_x/$(FAPbI_3)_{0.85}(MAPbBr_3)_{0.15}$ /TiO_2/Ag device is shown in **Figure 4**a. ALD method was chosen for depositing ETL, due to that ALD process was conformal deposition and independent of the roughness of the substrate.[31] The uniform thickness of TiO_2 (Figure 3b) also indicated that the ALD method was a more suitable strategy for the ETL deposition than spin-coating. We compared the *J–V* curves of ITO/NiO_x/$(FAPbI_3)_{0.85}(MAPbBr_3)_{0.15}$/$TiO_2$/Ag and ITO/$NiO_x$/$(FAPbI_3)_{0.85}$ $(MAPbBr_3)_{0.15}$/Ag, as listed in Figure 4b, where the single crystals have almost the same thickness and surface roughness. And the corresponding photovoltaic parameters are listed in Table S1 (Supporting Information). Without TiO_2 compact layer, the *J–V* curve was nearly a straight line with the considerably lower FF of 0.24. However, the J_{SC}, V_{oc}, and FF of the PSCSC were improved significantly by employing the ETL. Compared to the device with TiO_2, the device without TiO_2 had five times higher R_S. We speculated that when the ETL was absent, there was

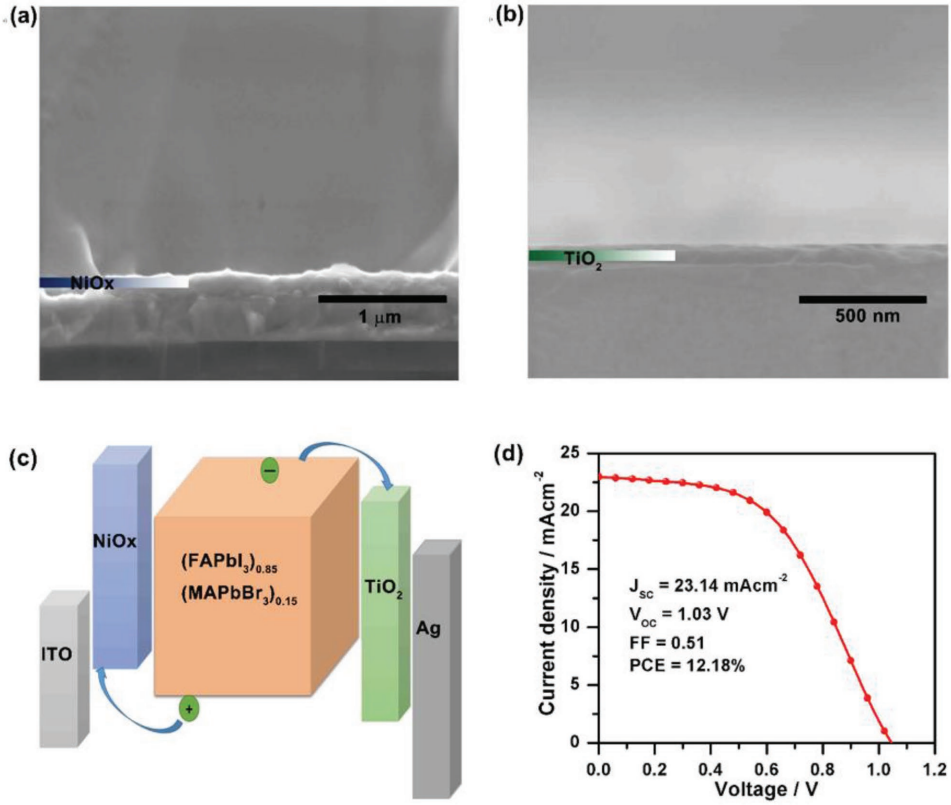

Figure 3. The cross-sectional SEM images of a) $NiO_x/(FAPbI_3)_{0.85}(MAPbBr_3)_{0.15}$ interface and b) $(FAPbI_3)_{0.85}(MAPbBr_3)_{0.15}/TiO_2$ interface; c) the band alignment and d) the *J–V* curve of the highest PCE of $ITO/NiO_x/(FAPbI_3)_{0.85}(MAPbBr_3)_{0.15}/TiO_2/Ag$.

significant reaction between Ag electrode and perovskite single crystal to form insulating AgI,[32] which resulted in the increase of the series resistance. Additionally, without ETL as hole-blocking layer, carriers recombine significantly at the perovskite/Ag interface, as shown in Figure 4b, which leads the decreased R_{Sh} and thus reduced V_{OC}. It should be mentioned that one of the reactants or the by-product, for example, H_2O and HCl, was considered to corrode the surface of single crystal or produce point defects.[33] However, the respectable V_{OC} and J_{SC} in the devices suggests that the corrosion from the ALD process is not so detrimental to the efficiency, which highlights the high tolerance of single-crystal perovskite film. ETL plays an important role in determining device performance. We thus investigated the impact of the ALD temperature and thickness of TiO_2 layer on the performance of devices. The *J–V* curves of resultant devices are shown in Figure S2 (Supporting Information). It showed the device with TiO_2 layer of 60 nm thick deposited at 100 °C exhibited the large FF and PCE.

The surface roughness and thickness of single crystals also have impact on the PCE. Since the relatively soft property of PDMS leads to the perovskite single crystal without smooth surface, the contact of $(FAPbI_3)_{0.85}(MAPbBr_3)_{0.15}/TiO_2/Ag$ has been affected. Figure 4c showed the *J–V* curves of PSCSCs based on single crystals with almost the same thickness but different surface roughness. The FF of device based on the single crystal with the larger surface roughness (Device A) was lower than that of device based on the smoother crystal (Device B), as presented in Table S2 and Figure S3 (Supporting Information), indicating the former situation had unfavorable electron extraction. We have also studied the impact of single-crystal thickness on the device performance. The *J–V* characteristics are shown in Figure 4d and Table S3 (Supporting Information). Their different efficiencies mainly resulted from the varied J_{SC}. As shown in Figure 4a, the effective area of single-crystal solar cells was smaller than the whole single crystal. Upon illumination, the carriers diffuse from the center of single crystals to the edge. It causes a part of photon carriers dissipated within the crystal. It can be inferred that the thinner single crystal provides fewer defects along the carrier pathway due to their small thickness. Therefore, the devices with the thinner single crystal had the better performance in average. However, the thickness of perovskite single crystal was just one of all the factors affecting the efficiency of devices. And the performance of the perovskite single-crystal solar cells is also affected by other factors, such as the contact of absorber with carrier transport layers. The contact quality further depends on the surface roughness of the single crystals. Yet, it is not trivial to control the surface roughness during single-crystal growth in our case. Therefore, the best PCE (12.18%) of devices, where the thickness of the single crystal was 24.5 μm, may result from the better contact originated from the smaller surface roughness.

It is also essential to investigate the role of HTL on device performance. The devices with the different processing temperature and thickness of NiO_x were carefully studied. The NiO_x layer with thickness of 95 nm annealed at 300 °C would lead the devices with high FF and thus PCE (Figure S4, Supporting

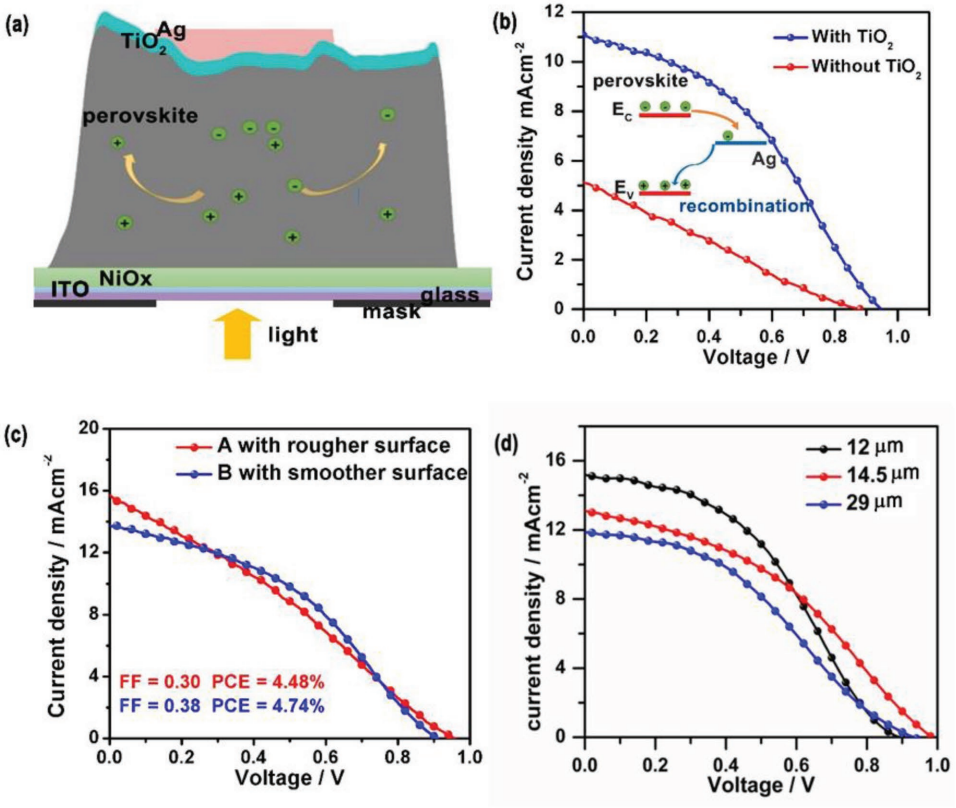

Figure 4. a) The proposed schematic diagram and the *J–V* curves of ITO/NiO_x/$(FAPbI_3)_{0.85}(MAPbBr_3)_{0.15}$/$TiO_2$/Ag devices: b) with TiO_2 layer of 60 nm thick deposited at 100 °C (blue line), and without TiO_2 layer (red line); c) where single crystal A (red line) and B (blue line) have almost the same thickness but different roughness; d) where single crystals have the different thickness (black line for 12 μm, red line for 14.5 μm, and blue line for 29 μm).

Information). Additionally, the rear electrode thickness was investigated. It showed that the different thickness of the dense Ag layers did not change the R_S and R_{Sh} of devices a lot due to their high conductivity (Figure S5, Supporting Information).

We listed the statistic photovoltaic data of ITO/NiO_x/$(FAPbI_3)_{0.85}(MAPbBr_3)_{0.15}$/$TiO_2$/Ag devices in Figure S6 (Supporting Information). It was observed that the efficiency changes mainly from the fluctuation of J_{SC} and FF, both of which are substantially influenced by the thickness and surface roughness of perovskite single crystal. The *J–V* curve and EQE data of the typical device are shown in Figure S7 (Supporting Information), and the integrated current density from EQE was 16.76 mA cm^{-2}, which was close to the measured J_{SC} (17.42 mA cm^{-2}).

The good hole extraction at the NiO_x/$(FAPbI_3)_{0.85}(MAPbBr_3)_{0.15}$ interface is also crucial to the high-efficiency devices. However, it is challenging to grow the pure phase $(FAPbI_3)_{0.85}(MAPbBr_3)_{0.15}$ single crystals without side phases. In some cases, yellow crystals were formed at the NiO_x/$(FAPbI_3)_{0.85}(MAPbBr_3)_{0.15}$ interfaces and edges (**Figure 5**a), which are assigned to PbI_2 phases with the diffraction peak at 12.8° and δ phase of $(FAPbI_3)_{1-x}(MAPbBr_3)_x$ perovskite with a small shoulder peak at 12.6°, respectively.[34,26] This may result from the nature of the mixed perovskite system, in which the precursors such as FAX, MAX (X = I, Br), PbI_2, $PbBr_2$ have different solubility in the γ-butyrolactone (GBL). It is generally believed that the different solubility of precursors in the solvent will ultimately influence the quality of final single crystals. For instance, the $MAPbBr_3$ single crystal was crystallized with opaque surface when adopted the antisolvent crystallization with molar ratio of MABr/$PbBr_2$, due to the lower solubility of $PbBr_2$ compared to MABr in N,N-dimethylformamide.[35] Similarly, a Cs-rich Cs_4PbBr_6 perovskite single crystal was also obtained as a result of the lower solubility of CsBr than that of $PbBr_2$ in dimethyl sulfoxide. Herein, to avoid the formation of side phases in the present study, the evaporation of GBL has been controlled carefully via adjusting the solution concentration and crystallization temperature, to allow the fast crystallization of pure phase $(FAPbI_3)_{0.85}(MAPbBr_3)_{0.15}$.

The *J–V* curves of device with and without side phases are shown in Figure 5c, and the photovoltaic parameters are listed in Table S5 (Supporting Information). An anomalous feature was observed in the device with side phases, which may be associated to the presence of hole blocks[36,37] at the NiO_x/$(FAPbI_3)_{0.85}(MAPbBr_3)_{0.15}$ interface, as shown in Figure 5a. Considering that the main component of side phase was PbI_2, we proposed the mechanism of hole extraction at the NiO_x/PbI_2/perovskite interface in Figure 5d. It clearly shows that the device with yellow crystals exhibits much larger R_S and slightly larger R_{Sh}. The valence band maximum (VBM) of PbI_2 (–5.75 eV)[2] was lower than that of NiO_x (–5.33 eV)[38] and that of perovskite (–5.65 eV),[39] so it introduced the energy barrier at the interface between perovskite and NiO_x. It effectively impeded the hole extraction, which thus led to the large R_S.

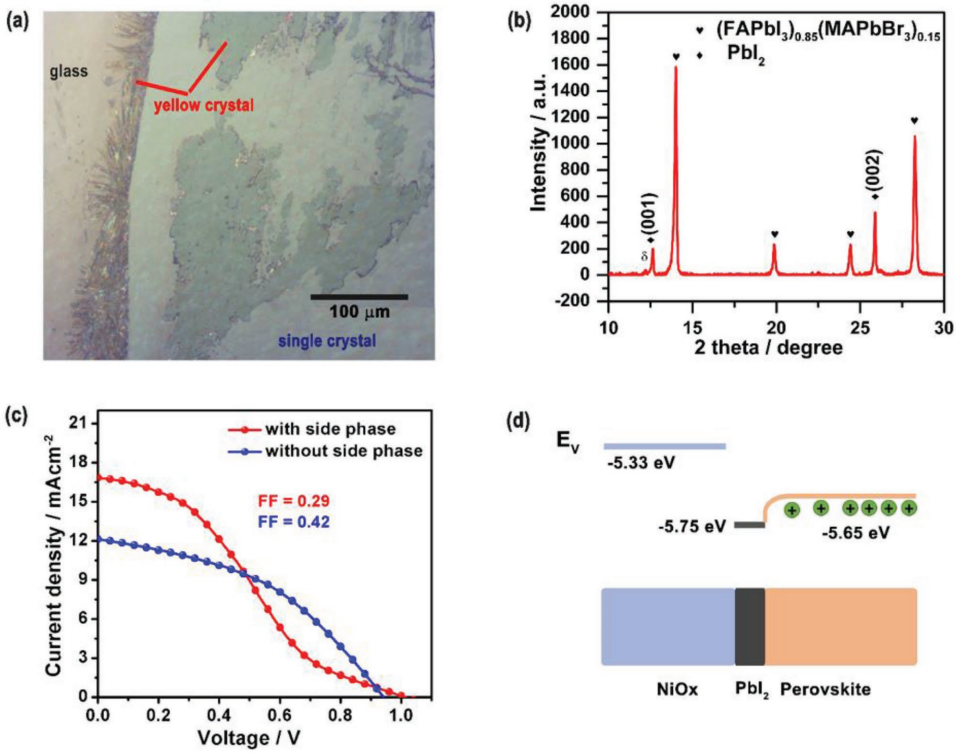

Figure 5. a) The photograph of $(FAPbI_3)_{0.85}(MAPbBr_3)_{0.15}$ single crystal on the NiO_x/ITO captured from the ITO side; b) powder X-ray diffraction of left crystals bladed from the substrate; c) the *J–V* curve of ITO/NiO_x/$(FAPbI_3)_{0.85}(MAPbBr_3)_{0.15}$/$TiO_2$/Ag device, and the single crystal with (red line) and without side phase (blue line); d) the barrier for hole extraction at the NiO_x/PbI_2/perovskite interface.

On the other hand, the barrier also prevented the direct contact between ITO and the absorber wherein NiO_x was missing. It reduced the recombination of holes to some extent and thus resulted in the slightly increased R_{Sh} in the device. Since the R_S enhancement is prevailing to R_{Sh} improvement, we observed FF decrease in the devices with yellow crystals. With respect to V_{OC}, the device with yellow crystals had larger R_{Sh} and therefore the less recombination and higher V_{OC}. And J_{SC} of device may be affected by several factors, which cannot be solely ascribed to the contribution of R_S and R_{Sh}.

In short, we could obtain the mixed halide $(FAPbI_3)_{0.85}(MAPbBr_3)_{0.15}$ perovskite single-crystal film with pure phase by carefully controlling the crystallization process, which addressed the most concerned part for mixed perovskite single-crystal film, and this method was suitable for the further application in PSCSC.

3. Conclusion

In conclusion, we synthesized the first mixed $(FAPbI_3)_{0.85}(MAPbBr_3)_{0.15}$ single-crystal film by the PDMS-assisted solvent evaporation method, and implemented it in the inverted ITO/NiO_x/$(FAPbI_3)_{0.85}(MAPbBr_3)_{0.15}$/$TiO_2$/Ag photovoltaic devices. An optimization of carrier behavior in the single-crystal solar cells leads to 12.18% PCE, which was also one of the high-efficiency PSCSCs up to now. The main factors that affect the device efficiency were thoroughly studied, including the interfaces of perovskite/TiO_2 and NiO_x/perovskite, the operation temperature, and thickness of transport layers, as well as the surface roughness and thickness of single crystal. Although ALD of TiO_2 layers may corrode perovskite single crystal, the employment of TiO_2 electron transport layer in the PSCSC device has good extraction ability and hole-blocking ability, which leads to the PSCSCs with higher FF and PCE. It was revealed that the crystallization process should also be controlled carefully to avoid the undesired yellow crystals as hole-blocking layer between NiO_x and $(FAPbI_3)_{0.85}(MAPbBr_3)_{0.15}$. Further efforts on device performance would be carried out to grow even thinner single crystals with smooth surface, and to reduce the surface recombination of single crystal by passivation. This work provides a full picture of interface engineering in single-crystal perovskite solar cells, which represents a significant step regarding fundamental understanding on perovskite single crystals and high device performance.

4. Characterizations

The surface roughness of single crystal was characterized by Scan Probe Microscope (SPI3800/SPA400). Single crystal on the substrates was scraped by blade, and then measured by single-crystal X-ray diffractometer with Mo Kα ray (λ = 0.071073 nm). Single crystals were scraped, grounded from single crystals in the glove box, and then measured by the Rigaku

D/MAX-2400 diffractometer for powder X-ray diffraction. We performed the steady-state photoluminescence (PL) and TRPL spectra of single crystal with the help of the steady-state spectrometer FLS980 (Edinburgh Instruments Ltd.) with 470 nm excitation wavelength. Absorption spectra of single crystal were measured by UV–visible–NIR spectrophotometer UH4150. The hole mobility of perovskite single crystal was obtained from the *I–V* curve of the ITO/NiO_x/perovskite single crystal/Au device with Keithley 4200 in the dark and room temperature according to SCLC measurement. All the *J–V* curves were measured under the mask with the area of 0.316 mm^2 under 1000 mW cm^{-2}. The SEM morphology was performed with the help of S4800. The thickness of single crystals was detected by DektakXT Stylus Profiler (Bruker). The laser scanning confocal microscope measurements were performed by A1R-si (Japan).

5. Experimental Section

Chemicals and Reagents: Nickel(II) nitrate hexahydrate ($Ni(NO_3)_2{\cdot}6H_2O$, Sigma, 99.999%), ethylene glycol ($C_2H_6O_2$, AR, 98%), diethylamine ($C_2H_8N_2$, AR), lead (II) iodide (PbI_2, Alfa, 99.9985%), lead(II) bromide ($PbBr_2$, sigma, 99.999%), methylamine (CH_3NH_2, 40%w/w aq. soln.), formamidine acetate salt (FAAc, Aladdin, 99%), hydroiodic acid (HI, Alfa Aesar, 57% w/w aq. soln., stab with 1.5% hypophosphorous acid), hydrobromic acid (HBr, AR, 48% w/w), gamma-butyrolactone ($C_4H_6O_2$, GBL, Aladdin, 99%), silicone elastomer base and curing agent (Dowcorning, 184), and $TiCl_4$.

Synthesis of CH_3NH_3Br (MABr) and $CH(NH_2)_2I$ (FAI): MABr was synthesized by stirring the mixture of CH_3NH_2 (30 mL) and HBr (36 mL) in a 250 mL three-neck round bottom flask at 0 °C ice bath for 2 h. The solvent was evaporated, and the remains were washed with diethyl ether and then filtered. Next, the product was redissolved in ethanol and recrystallized, and washed with diethyl ether for three times. The final white crystals were dried in a vacuum oven for 24 h. FAAc (14 g) and HI (32.3 mL) were the raw materials for the synthesis of FAI, and the synthesis strategy was similar to that of MABr.[40]

Synthesis of Polydimethylsiloxane: Silicone elastomer base and curing agent were mixed by weight ratio of 10:1 in beaker,[41] and stirred intensely for 0.5 h to produce many bubbles. Then the mixture was put in the vacuum oven to remove bubbles. The mixture was spread on the glass substrate and baked at 80 °C for 2 h.

Preparation of Inverted Single-Crystal Solar Cells: ITO glass was cleaned with acetone, ethanol, and isopropanol in turn. After UV–ozone treatment, ITO was deposited with NiO_x[42,43] by spin-coating (5000 rpm for 40 s) the filtered solution of nickel (II) nitrate hexahydrate, ethylene glycol, and diethylamine, and then baked at 300 °C for 1 h. Next, PDMS was spread on the NiO_x/ITO, and then injected perovskite solution, which consists of FAI (87.72 mg), PbI_2 (235.16 mg), MABr (10.09 mg), $PbBr_2$ (33.22 mg), and GBL (0.5 mL). After heating the solution at 80 °C for 1.5 h, regular single crystal was obtained. Then the high-temperature resistant tape with 0.316 mm^2 hole was taped on the single crystal for the TiO_2 deposition mask. And then 60 nm TiO_2 was deposited by ALD with $TiCl_4$ and H_2O on the single crystal, and finally 150 nm Ag electrode by vapor deposition.

Supporting Information

Supporting Information is available from the Wiley Online Library or from the author.

Acknowledgements

The authors acknowledge the support from the National Natural Science Foundation of China (51672008, 51722201, and 91733301), National Key Research and Development Program of China (Grant No. 2017YFA0206701), and Young Talent Thousand Program. The authors thank Prof. X. W. Zhan (College of Engineering, Peking University) for step profiler measurement, Prof. Z. F. Dai (College of Engineering, Peking University) for optical microscope, and Prof. J. Pei (College of Chemistry and Molecular Engineering, Peking University) for SCLC measurement, respectively. The authors highly appreciated the help from Prof. Liang Li and Fengren Cao (Soochow University) regarding ALD TiO_2 during revision process. The authors thank Yihua Chen for drawing the schematic diagram.

Conflict of Interest

The authors declare no conflict of interest.

Keywords

$(FAPbI_3)_{0.85}(MAPbBr_3)_{0.15}$, carrier dynamics, polydimethylsiloxane (PDMS), single-crystal solar cells, TiO_2

Received: February 9, 2018
Revised: April 3, 2018
Published online:

[1] S. D. Stranks, G. E. Eperon, G. Grancini, C. Menelaou, M. J. P. Alcocer, T. Leijtens, L. M. Herz, A. Petrozza, H. J. Snaith, *Science* **2013**, *342*, 341.
[2] Q. Chen, H. Zhou, T. B. Song, S. Luo, Z. Hong, H.S. Duan, L. Dou, Y. Liu, Y. Yang, *Nano Lett.* **2014**, *14*, 4158.
[3] W. J. Yin, T. Shi, Y. Yan, *Adv. Mater.* **2014**, *26*, 4653.
[4] C. Muthu, S. Agarwal, A. Vijayan, P. Hazra, K. B. Jinesh, V. C. Nair, *Adv. Mater. Interfaces* **2016**, *3*, 1600092.
[5] H. Zhu, Y. Fu, F. Meng, X. Wu, Z. Gong, Q. Ding, M. V. Gustafsson, M. T. Trinh, S. Jin, X. Y. Zhu, *Nat. Mater.* **2015**, *14*, 636.
[6] W. Pan, H. Wu, J. Luo, Z. Deng, C. Ge, C. Chen, X. Jiang, W. J. Yin, G. Niu, L. Zhu, L. Yin, Y. Zhou, Q. Xie, X. Ke, M. Sui, J. Tang, *Nat. Photonics* **2017**, *11*, 726.
[7] Z. Xiao, R. A. Kerner, L. Zhao, N. L. Tran, K. M. Lee, T. W. Koh, G. D. Scholes, B. P. Rand, *Nat. Photonics* **2017**, *11*, 108.
[8] W. S. Yang, B. W. Park, E. H. Jung, N. J. Jeon, Y. C. Kim, D. U. Lee, S. S. Shin, J. Seo, E. K. Kim, J. H. Noh, S. I. Seok, *Science* **2017**, *356*, 1376.
[9] Q. Dong, Y. Fang, Y. Shao, P. Mulligan, J. Qiu, L. Cao, J. Huang, *Science* **2015**, *347*, 967.
[10] D. Shi, V. Adinolfi, R. Comin, M. Yuan, E. Alarousu, A. Buin, Y. Chen, S. Hoogland, A. Rothenberger, K. Katsiev, Y. Losovyj, X. Zhang, P. A. Dowben, O. F. Mohammed, E. H. Sargent, O. M. Bakr, *Science* **2015**, *347*, 519.
[11] J. Huang, Y. Shao, Q. Dong, *J. Phys. Chem. Lett.* **2015**, *6*, 3218.
[12] P. Guggilla, A. Chilvery, K. Bhat, E. J. Bernardez, *J. Photonic Mater. Technol.* **2016**, *2*, 25.
[13] W. Peng, X. Miao, V. Adinolfi, E. Alarousu, O. El Tall, A. H. Emwas, C. Zhao, G. Walters, J. Liu, O. Ouellette, J. Pan, B. Murali, E. H. Sargent, O. F. Mohammed, O. M. Bakr, *Angew. Chem.* **2016**, *55*, 10686.
[14] M. I. Saidaminov, A. L. Abdelhady, B. Murali, E. Alarousu, V. M. Burlakov, W. Peng, I. Dursun, L. Wang, Y. He, G. Maculan, A. Goriely, T. Wu, O. F. Mohammed, O. M. Bakr, *Nat. Commun.* **2016**, *6*, 7586.
[15] Y. Liu, Z. Yang, D. Cui, X. Ren, J. Sun, X. Liu, J. Zhang, Q. Wei, H. Fan, F. Yu, X. Zhang, C. Zhao, S. F. Liu, *Adv. Mater.* **2015**, *27*, 5176.

[16] Z. Lian, Q. Yan, T. Gao, J. Ding, Q. Lv, C. Ning, Q. Li, J. L. Sun, *J. Am. Chem. Soc.* **2017**, *139*, 3320.
[17] Y. Dang, Y. Liu, Y. Sun, D. Yuan, X. Liu, W. Lu, G. Liu, H. Xia, X. Tao, *CrystEngComm* **2015**, *17*, 665.
[18] T. Ye, W. Fu, J. Wu, Z. Yu, X. Jin, H. Chen, H. Li, *J. Mater. Chem. A* **2016**, *4*, 1214.
[19] Q. Dong, J. Song, Y. Fang, Y. Shao, S. Ducharme, J. Huang, *Adv. Mater.* **2016**, *28*, 2816.
[20] W. Peng, L. Wang, B. Murali, K. T. Ho, A. Bera, N. Cho, C. F. Kang, V. M. Burlakov, J. Pan, L. Sinatra, C. Ma, W. Xu, D. Shi, E. Alarousu, A. Goriely, J. H. He, O. F. Mohammed, T. Wu, O. M. Bakr, *Adv. Mater.* **2016**, *28*, 3383.
[21] H. S. Rao, B. X. Chen, X. D. Wang, D. B. Kuang, C. Y. Su, *Chem. Commun.* **2017**, *53*, 5163.
[22] J. Zhao, G. Kong, S. Chen, Q. Li, B. Huang, Z. Liu, X. San, Y. Wang, C. Wang, Y. Zhen, H. Wen, P. Gao, J. Li, *Sci. Bull.* **2017**, *62*, 1173.
[23] Z. Chen, Q. Dong, Y. Liu, C. Bao, Y. Fang, Y. Lin, S. Tang, Q. Wang, X. Xiao, Y. Bai, Y. Deng, J. Huang, *Nat. Commun.* **2017**, *8*, 1890.
[24] K. T. Cho, S. Paek, G. Grancini, C. R. Carmona, P. Gao, Y. Lee, M. K. Nazeeruddin, *Energy Environ. Sci.* **2017**, *10*, 621.
[25] Y. X. Chen, Q. Q. Ge, Y. Shi, J. Liu, D. J. Xue, J. Y. Ma, J. Ding, H. J. Yan, J. S. Hu, L. J. Wan, *J. Am. Chem. Soc.* **2016**, *138*, 16196.
[26] L. Q. Xie, L. Chen, Z. A. Nan, H. X. Lin, T. Wang, D. P. Zhan, J. W. Yan, B. W. Mao, Z. Q. Tian, *J. Am. Chem. Soc.* **2017**, *139*, 3320.
[27] Q. Han, S. H. Bae, P. Sun, Y. T. Hsieh, Y. M. Yang, Y. S. Rim, H. Zhao, Q. Chen, W. Shi, G. Li, Y. Yang, *Adv. Mater.* **2016**, *28*, 2253.
[28] M. He, B. Li, X. Cui, B. Jiang, Y. He, Y. Chen, D. O'Neil, P. Szymanski, M. A. Ei Sayed, J. Huang, Z. Lin, *Nat. Commun.* **2017**, *8*, 16045.
[29] http://pveducation.org/pvcdrom/solar-cell-operation/series-resistance **2018**, *4*.
[30] H. Peng, W. Sun, Y. Li, S. Ye, H. Rao, W. Yan, H. Zhou, Z. Bian, C. Huang, *Nano Res.* **2016**, *9*, 2960.
[31] V. Zardetto, B. L. Williams, A. Perrotta, F. Di Giacomo, M. A. Verheijen, R. Andriessen, W. M. M. Kessels, M. Creatore, *Sustainable Energy Fuels* **2017**, *1*, 30.
[32] Y. Kato, L. K. Ono, M. V. Lee, S. Wang, S. R. Raga, Y. Qi, *Adv. Mater. Interfaces* **2015**, *2*, 1500195.
[33] B. Murali, S. Dey, A. L. Abdelhady, W. Peng, E. Alarousu, A. R. Kirmani, N. Cho, S. P. Sarmah, M. R. Parida, M. I. Saidaminov, A. A. Zhumekenov, J. Sun, M. S. Alias, E. Yengel, B. S. Ooi, A. Amassian, O. M. Bakr, O. F. Mohammed, *ACS Energy Lett.* **2016**, *1*, 1119.
[34] Y. He, Y. Jin, B. Chen, Z. He, L. Wang, *Cryst. Res. Technol.* **2015**, *50*, 823.
[35] H. Wei, Y. Fang, P. Mulligan, W. Chuirazzi, H. H. Fang, C. Wang, B. R. Ecker, Y. Gao, M. A. Loi, L. Cao, J. Huang, *Nat. Photonics* **2016**, *10*, 333.
[36] A. Kumar, S. Sista, Y. Yang, *J. Appl. Phys.* **2009**, *105*, 094512.
[37] J. J. Shi, H. Y. Wei, L. F. Zhu, X. Xu, Y. Z. Xu, S. T. Lu, H. J. Wu, Y. H. Luo, D. M. Li, Q. B. Meng, *Acta Phys. Sin.* **2015**, *64*, 038402.
[38] J. Cao, H. Yu, S. Zhou, M. Qin, T. K. Lau, X. Lu, N. Zhao, C. P. Wong, *J. Mater. Chem. A* **2017**, *5*, 11071.
[39] K. H. Lin, A. Prlj, C. Corminboeuf, *J. Phys. Chem. C* **2017**, *121*, 21729.
[40] W. S. Yang, J. H. Noh, N. J. Jeon, Y. C. Kim, S. Ryu, J. Seo, S. I. Seok, *Science* **2015**, *348*, 1234.
[41] P. Khoram, S. Brittman, W. I. Dzik, J. N. H. Reek, E. C. Garnett, *J. Phys. Chem. C* **2016**, *120*, 6475.
[42] G. E. Eperon, T. Leijtens, K. A. Bush, R. Prasanna, T. Green, J. T. W. Wang, D. P. McMeekin, G. Volonakis, R. L. Milot, R. May, A. Palmstrom, D. J. Slotcavage, R. A. Belisle, J. B. Patel, E. S. Parrott, R. J. Sutton, W. Ma, F. Moghadam, B. Conings, A. Babayigit, H. G. Boyen, S. Bent, F. Giustino, L. M. Herz, M. B. Johnston, M. D. McGehee, H. J. Snaith, *Science* **2016**, *354*, 861.
[43] J. W. Jung, C. C. Chueh, A. K. Jen, *Adv. Mater.* **2015**, *27*, 7874.

